Journal of Energy Storage 78 (2024) 110043

Contents lists available at ScienceDirect

Journal of Energy Storage

journal homepage: www.elsevier.com/locate/est

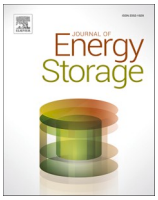

Research papers

Performance study of a thermochemical energy storage reactor embedded with a microchannel tube heat exchanger for water heating

Yong Zhang, Mingke Hu *, Ziwei Chen, Yuehong Su *, Saffa Riffat

Department of Architecture and Built Environment, University of Nottingham, University Park, Nottingham NG7 2RD, UK

ARTICLE INFO

Keywords:
Thermochemical energy storage
Microchannel tube heat exchanger
Heat recovery
Thermal efficiency

ABSTRACT

Thermochemical energy storage (TCES) provides a promising solution to addressing the mismatch between solar thermal production and heating demands in buildings. However, existing air-based open TCES systems face practical challenges in integrating with central water heating systems and controlling the supply temperature. To overcome these limitations, a novel water-based TCES-HEX-HRU system is proposed in this study, which integrates a water-to-air microchannel tube heat exchanger (HEX) and an air-to-air heat recovery unit (HRU). A comprehensive evaluation of the TCES-HEX-HRU system is conducted numerically using a COMSOL model, including a comparative assessment for different TCES system configurations. The results demonstrate that the TCES-HEX-HRU system achieves an overall thermal efficiency of 82.35 %, marking a substantial 69 percentage points improvement over the TCES-HEX system. Although slightly lower than the typical air-based TCES system without HEX and HRU by 15.44 percentage points, the TCES-HEX-HRU system can be a practically promising and viable choice for applications in central heating systems. Numerical investigations indicate that the thermal performance of the system is influenced by the inlet conditions of airflow and waterflow. Moreover, increasing the number of water channels in the HEX of the TCES-HEX-HRU system enhances heat transfer but reduces the amount of heat released by TCES composite materials, resulting in a maximum overall thermal efficiency of 92.09 % with 35 channels and a peak outlet water temperature of 33.67 °C at with 30 channels. However, further increases in the number of channels lead to a decline in overall thermal efficiency and outlet water temperature. Changes in the width of water channels in the HEX have a minor impact on the highest outlet water temperature and overall thermal efficiency, while affecting the volume of the TCES composite materials.

1. Introduction

Currently, the world is facing an unprecedented global energy crisis, with European countries being at the forefront [1]. Within these countries, the residential sector plays a significant role as it accounts for approximately one-third of the total energy consumption across all sectors [2]. In the UK, over 80 % of the energy demand in the residential sector is attributed to heating applications, with approximately 60 % of this demand being met by fossil fuels [3,4]. As a result of this energy crisis, around 4.5 million households in the UK are experiencing fuel shortages and living in cold conditions [5].

To address these challenges, it is crucial to promote the increased adoption of renewable and alternative energy technologies, particularly solar energy, in domestic heating applications [6]. However, the intermittency of solar energy restricts its widespread utilization in domestic heating applications [7]. To fully harness the potential of solar energy for residential heating, the development of energy storage systems is necessary, particularly for long-term storage to store excess solar energy accumulated over extended periods (3–6 months) during summer [8].

Thermal energy storage (TES) technologies encompass three main categories: sensible thermal energy storage (STES) [9], latent thermal energy storage (LTES) [10], and thermochemical heat storage (TCES) [11]. Among these, TCES technology stands out due to its higher energy storage density (ESD, approximately 200–700 kWh·m^{-3}) [12], smaller volume [13] and negligible heat loss during storage [14]. These advantages position TCES technology as a highly promising solution for seasonal energy storage in the residential sector, especially in situations where space is limited [15].

* Corresponding authors.
E-mail addresses: mingke.hu@nottingham.ac.uk (M. Hu), yuehong.su@nottingham.ac.uk (Y. Su).

https://doi.org/10.1016/j.est.2023.110043
Received 6 July 2023; Received in revised form 13 November 2023; Accepted 6 December 2023
Available online 12 December 2023

Nomenclature

A_{freq}	Pre-exponential Arrhenius factor, s^{-1}	ρ	Density, $kg{\cdot}m^{-3}$
C	Specific heat, $J{\cdot}g^{-1}{\cdot}K^{-1}$	ε	porosity
c	Mole concentration, $mol{\cdot}m^{-3}$	α	Reaction conversion degree
D_g	Gas diffusivity in reactive bed, $m^2{\cdot}s^{-1}$	η	Efficiency, %
d	Thickness or depth, m	μ	Dynamic viscosity, Pa·s
E_a	Arrhenius activation energy, $J{\cdot}mol^{-1}$	λ	Thermal conductivity, $W{\cdot}m^{-1}{\cdot}K^{-1}$
ΔH_r	Enthalpy, $J{\cdot}mol^{-1}$		
h	Heat transfer coefficient, $W{\cdot}m^{-2}{\cdot}K^{-1}$	Subscripts	
k	Permeability, m^2	a	Air
M	Molecular mass, $g{\cdot}mol^{-1}$	ab	Heat absorbed
$\dot{m}$	Mass flow rate, $kg{\cdot}s^{-1}$	amb	Ambient
Nu	Nusselt number	Al	Aluminium substrate
P	Pressure, Pa	dis	Discharging
Pr	Prandtl number	eff	Effective
$\dot{q}$	Volumetric heat source, $W{\cdot}m^{-3}$	eq	Equilibrium state
Q	Heat, J	f	Final
R	Universal gas constant, $J{\cdot}mol^{-1}{\cdot}K^{-1}$	i	Initial
Ra	Rayleigh number	in	Inlet
R_{kin}	Kinetic factor, s^{-1}	int	interval
ΔS_r	Entropy, $J{\cdot}mol^{-1}{\cdot}K^{-1}$	ins	Insulation plate
S_w	Mass source of water vapor, $kg{\cdot}m^{-3}{\cdot}s^{-1}$	kin	Kinetic
T	Temperature, K or °C	w	Water
t	Time, min	re	Heat release
$\vec{u}$	Velocity vector, $m{\cdot}s^{-1}$	out	Outlet
V	Volume of salt bed, m^3		
z	Stoichiometric number		

Thermochemical materials (TCMs) play a crucial role in TCES systems. Salt hydrates (e.g., $MgCl_2{\cdot}6H_2O$ [16], $CaCl_2{\cdot}6H_2O$ [17], $SrBr_2{\cdot}6H_2O$ [18], and $MgSO_4{\cdot}7H_2O$ [19]) are typical TCMs that offer several advantages, including high ESD [20], low cost [21], and non-toxicity [22]. In addition, their regeneration temperature is below 150 °C, making them suitable for solar energy storage [23]. Salt hydrates utilize reversible solid-gas reactions to store or release heat during charging (i.e., dehydration) or discharging (i.e., hydration) processes [24]. The working principle is illustrated in in Fig. 1.

In the solar-driven salt hydrate-based TCES system, the salt hydrate ($salt{\cdot}nH_2O$) absorbs solar heat and decomposes into salt and water vapor during the charging process, Conversely, the reverse reaction allows for the recombination of the salt and water vapor, accompanied by heat release during the discharging process [25]. The reversible solid-gas chemical reaction of the salt hydrate is described as follows:

$$Salt{\cdot}nH_2O_{(solid)} + \Delta H \underset{discharging}{\overset{charging}{\rightleftarrows}} Salt{\cdot}(n-m)H_2O_{(solid)} + mH_2O_{(gas)} \quad (1)$$

$CaCl_2$ has garnered widespread attention as a commonly used salt in TCMs. Several factors contribute to its appeal. To begin with, $CaCl_2$ is easily accessible and comparatively cost-effective (priced at 1–5£/kg). Additionally, it demonstrates exceptional water absorption capacity and energy storage density, showcasing remarkable energy storage potential. Moreover, when compared to other salt hydrates, $CaCl_2$ exhibits superior chemical stability, low corrosive tendencies, and non-toxic attributes. Notably, it can undergo dehydration reactions at relatively modest temperatures (below 100 °C), making it highly suitable for low-temperature energy storage applications [26]. This amalgamation of qualities positions $CaCl_2$ as a highly promising salt hydrate, especially well-suited for a diverse range of applications in the context of building-related thermal energy storage. Table 1 presents characteristics of several commonly used salts in TCES system for reference.

However, the use of pure salt in TCES systems has limitations, particularly in terms of its deliquescence relative humidity (DRH). While desorption and adsorption processes can contribute to agglomeration

Table 1
Characteristics of several commonly used salts in TCES system.

Salt	Energy storage density ($kWh{\cdot}m^{-3}$)	Dehydration temperature (°C)	Cost (£·kg^{-1})	Reference
K_2CO_3	361	93	1–5	[27]
$CuCl_2$	483	53	10–50	[28]
$MgCl_2$	694	150	1–10	[27]
$SrBr_2$	628	88	50–200	[20]
$MgSO_4$	558	85	1–5	[29]
$CaCl_2$	750	32	1–5	[30]

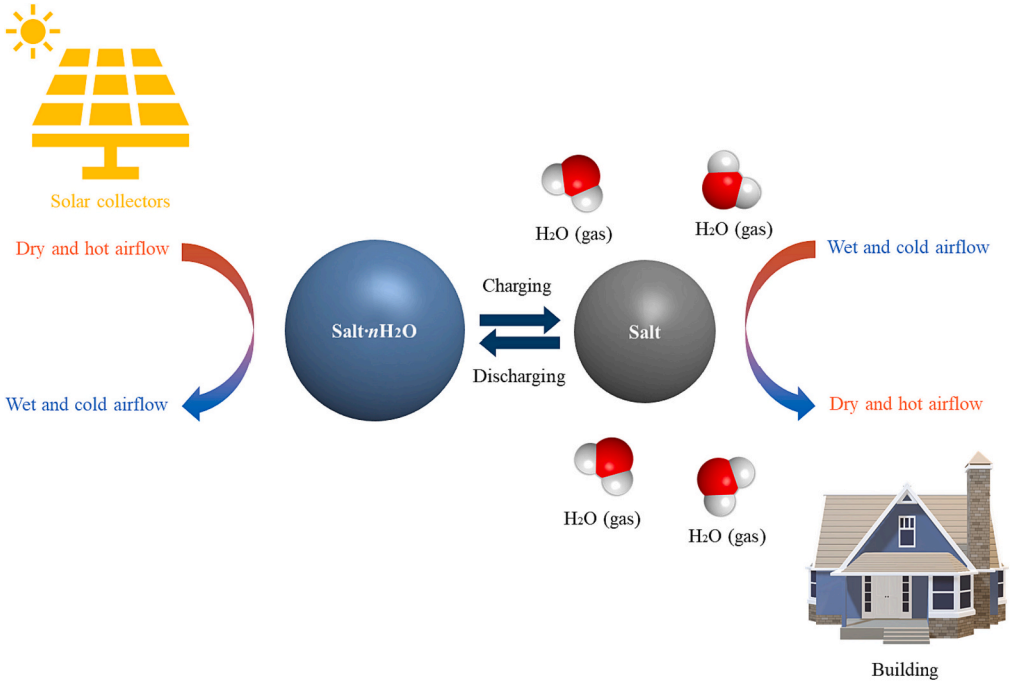

Fig. 1. Schematic diagram of the reaction process of salt hydrates for solar energy storage in building applications.

and swelling of salt hydrates, it is imperative to highlight that deliquescence of salt hydrate significantly exacerbates these phenomena when the relative humidity of work airflow exceeds the DRH [31]. These occurrences pose impediments to mass transfer and the overall cyclic stability of the system [26]. Concurrently, the formation of salt solutions due to the deliquescence of salt hydrates can lead to corrosion of reactor components, thereby diminishing the reactor's lifespan [21]. To address these, the formation of TCES composite materials through impregnation has been proposed. This involves attaching salts to the pore surface of porous materials such as zeolites [32], expanded vermiculite [33], expanded graphite [26] and silica gel [34]. TCES composite materials offer the advantage of combining the benefits of both salts and porous materials while mitigating their respective drawbacks [35]. The numerous micron-sized pores in TCES composite materials facilitate gas diffusion and promote mass transfer, thereby alleviating agglomeration and melting of salt during the discharge process [36]. Additionally, porous matrices have been used to enhance the thermal conductivity of TCMs. For example, the thermal conductivity of a TCES composite material composed of expanded natural graphite treated with sulfuric acid and $SrBr_2$ can be significantly higher than that of pure $SrBr_2$ [37]. Vermiculite is a naturally non-toxic mineral known for its lightweight and chemical inertness. It has become a favoured option as the primary matrix for composite materials [38]. TCES composite materials consisting of vermiculite and calcium chloride exhibit the most promising water uptake capability and excellent energy storage density when compared to other commonly used TCES composite materials. It has been demonstrated to possess great potential in open TCES systems [33]. A performance comparison of several commonly used composite materials is presented in Table 2.

In general, TCES systems can be classified into two types: open and closed systems [41]. Open systems use water vapor as both the reactant and product, which is obtained from the atmosphere during discharging and released back into the atmosphere during charging [42]. Water vapor serves as the medium for heat and mass transfer, eliminating the need for additional components in the system [43]. Open systems offer advantages in terms of structural simplicity, volumetric energy storage density, cost, and efficiency [13,44,45]. On the other hand, closed systems require an evaporator/condenser to generate and collect vapor during the discharge and charging processes, as well as a heat exchanger unit for heat transfer to external applications [46]. In addition, closed systems also require a high vacuum and sealed integrity in the reactor, making them more complex and expensive [47]. However, closed systems have the advantage of minimal environmental pollution due to their high seal integrity [36]. Considering the environmentally friendly nature of salt hydrates, open structures are more commonly used for salt hydrate-based TCES systems [48].

To enhance the performance of open TCES systems, researchers have made various attempts to optimize the structure of the reaction bed, operational parameters, and system configuration. Concerning the reaction bed, the long vapor permeation distance in the reaction hinders the transfer of water vapor, leading to the agglomeration and melting of TCMs, thereby affecting the system efficiency [31]. In recent years, novel reactor bed structures, such as honeycomb [49], multi-module [50], and copper mesh-packed structures [51], have been proposed to enhance the heat and mass transfer performance and improve the overall performance of TCES systems [24,52]. Operational parameters also play a crucial role in influencing the efficiency of TCES systems. Appropriate operational parameters, including temperature, airflow velocity, and operating pressure, have been demonstrated to maintain high system performance [8,16,24]. Furthermore, the optimization of system configuration has gained significant attention. The incorporation of supplementary components such as air-source heat pumps, solar collectors, and heat recovery units can significantly reduce the external energy consumption during the charging process of TCES systems, resulting in the improved thermal efficiency and performance coefficient [53,54].

Table 2
Performance comparison of several commonly used TCES composite materials.

Host matrix	Salt	Salt content (wt%)	Water uptake capability ($g \cdot g^{-1}$)	Energy storage density ($J \cdot g^{-1}$)	Reference
Vermiculite	$CaCl_2$	72	1.04	1493	This study
Vermiculite	$SrBr_2$	58	0.53	1650	[37]
Vermiculite	$LiNO_3$	63	0.50	900	[39]
Silica-gel	$CaCl_2$	43	0.40	1080	[40]
Diatomite	$CaCl_2$	33	0.82	1520	[21]

The current mainstream research on open TCES systems primarily focuses on using air as the medium for providing thermal energy to external spaces or applications directly. However, the utilization of water as the medium in open TCES systems has not been extensively studied. In contrast, a significant proportion (i.e., 95 %) of households in regions like the UK utilize central heating systems that circulate water to heat radiators [55]. While using air as a heat transfer medium for space heating is efficient and rapid, air-based TCES systems operate independently and cannot be easily integrated with existing central heating systems. It also requires the installation of a number of air ducts within buildings, which is challenging when renovating older building structures. Moreover, during the initial stage of the discharging process, the air-based TCES systems may possibly encounter the problem of overheating supply air [56].

In response to the limitations faced by conventional TCES systems, a novel TCES system has been introduced in this study, referred to as the TCES-HEX-HRU system. This novel system integrates a TCES reactor, an internal water-to-air microchannel tube heat exchanger (HEX), and an external air-to-air heat recovery unit (HRU) to revolutionize the way of managing and harnessing thermal energy of open-type TCES system. The novel system facilitates the transfer of heat released by TCES composite materials into the water within the embedded HEX, subsequently directing it into the central hot water system of the building. This approach minimizes the necessity for extensive retrofitting of the existing residential buildings where water primarily serves as the heat transfer medium for space heating systems. Furthermore, as the heated water in the TCES-HEX-HRU system is conveyed to the central hot water buffer tank rather than terminal radiators in individual rooms, concerns related to the potential discomfort resulting from space overheating during the initial discharging of the air-based TCES system are alleviated. Moreover, the HRU component at the system's end effectively harnesses the residual heat from the reactor's exhaust airflow to preheat the ambient air entering the system, ensuring the effective utilization of the heat generated by the salt hydrate instead of allowing it to dissipate extensively into the environment.

To validate the feasibility of the TCES-HEX-HRU system during the discharging process, a dynamic model of a small-scale system has been developed using COMSOL. Furthermore, this study conducts a comprehensive parametric analysis to explore the impact of various operational and structural parameters on the discharging performance of this pioneering system. This innovative integration of components, efficient heat transfer, and heat recovery mechanisms make the TCES-HEX-HRU system a promising solution for thermochemical energy storage.

2. System description

The schematic diagram of the TCES-HEX-HRU system proposed in this study is presented in Fig. 2. This system mainly consists of a TCES reactor with an inserted water-to-air microchannel tube heat exchanger (HEX) unit, an air-to-air heat recovery unit (HRU), a duct fan, and an ultrasonic humidifier. During the discharging process, low-temperature ambient air enters HRU and is preheated by the hot exhaust air from the TCES reactor. Subsequently, the preheated airflow is humidified by the

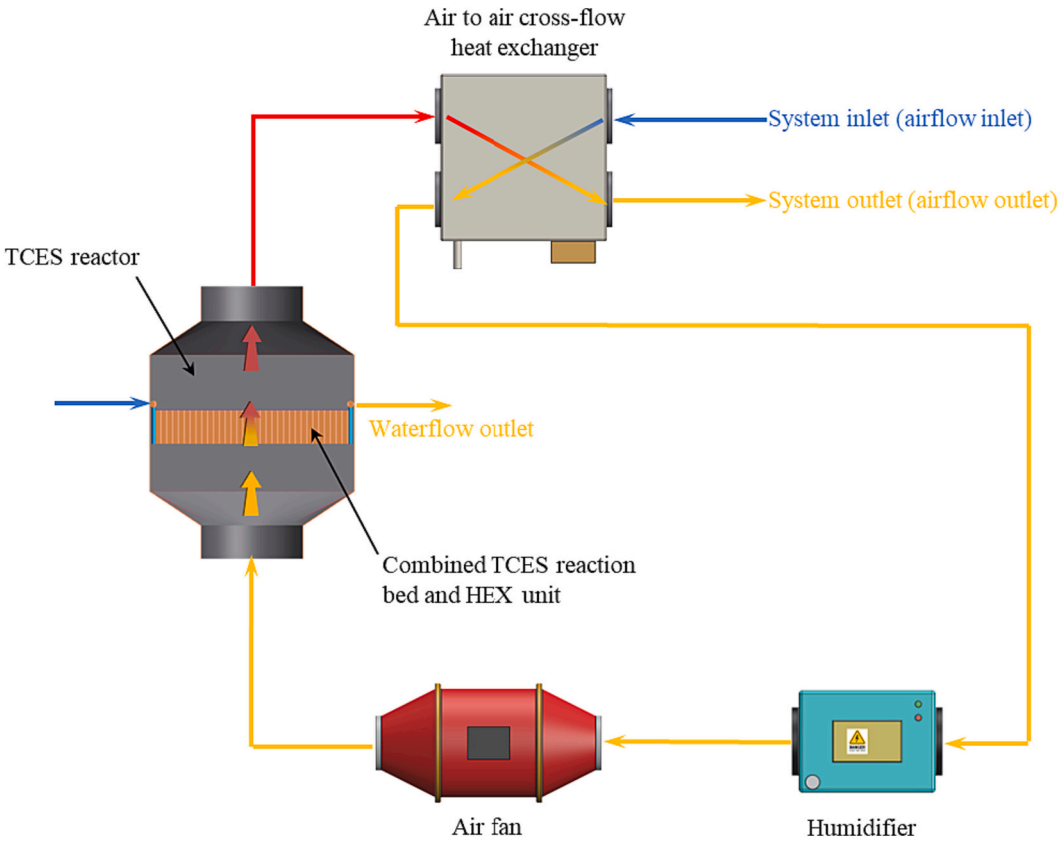

Fig. 2. Schematic of the TCES-HEX-HRU system.

ultrasonic humidifier. After that, the humidified airflow enters the TCES reactor and flows upwards through the reaction bed, where the moisture in the airflow is absorbed by the TCES composite materials, accompanied by abundant absorption heat being released. Part of the heat is transferred to the water through HEX and flows into the building central water heating system, while the remaining heat is absorbed by the airflow. Finally, the heated airflow is directed to HRU for heat recovery before being exhausted into the environment.

The 3D structure of the combined TCES reaction bed and HEX unit within the TCES reactor is depicted in Fig. 3. The reaction bed has dimensions of 0.28 m × 0.28 m × 0.05 mm (length × width × height) and consists of 10 water-to-air water channels (flat microchannel tubes) that

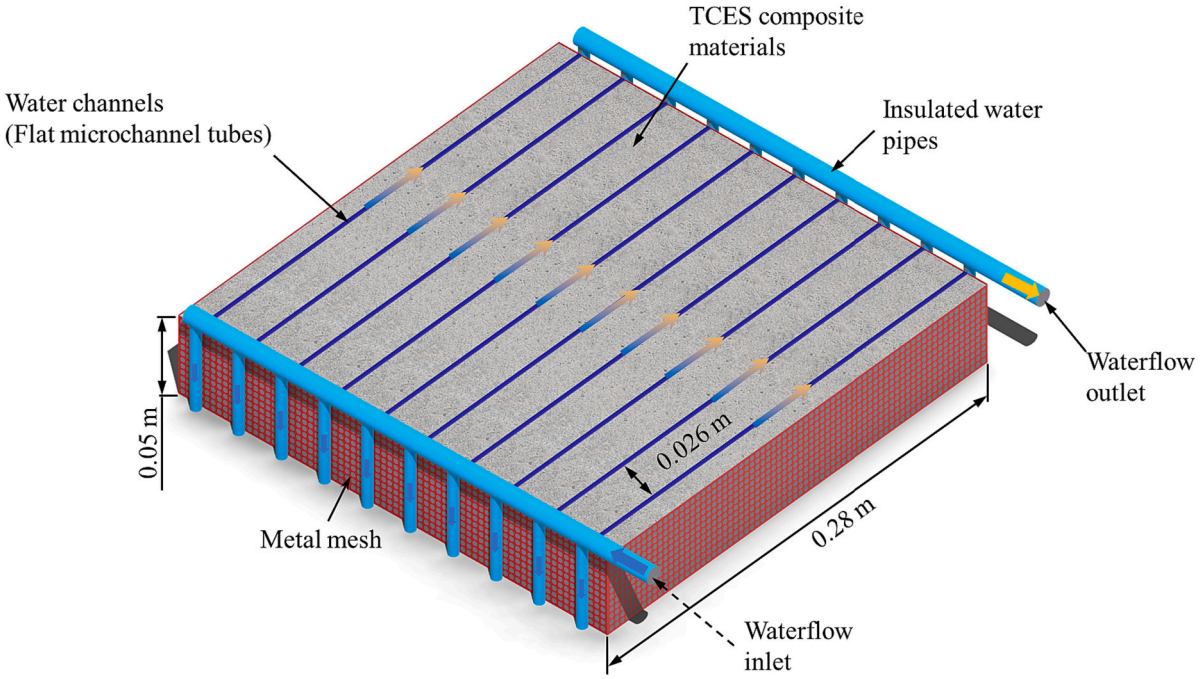

Fig. 3. Schematic of the combined TCES reaction bed and HEX unit.

traverse the entire bed. Each water channel has a width of 0.002 m, a height of 0.05 m, and a spacing of 0.026 m between water channels. Water is utilized as the heat exchange medium inside HEX. The residual space within the reaction bed was occupied by TCES composite materials, specifically consisting of vermiculite and $CaCl_2$ in this investigation. These vermiculite-$CaCl_2$ TCES composite materials were prepared using the conventional dry impregnation technique. The TCES composite materials display varying axial lengths, ranging from 3 to 8 mm, with corresponding cross-sectional areas spanning from 0.64 to 2 cm^2. It is noteworthy that these materials exhibit a porosity of 0.64 and a permeability of 8.24×10^{-6} m^2.

3. Mathematical model

This study develops a mathematical model to quantitatively assess the discharging performance of the proposed TCES-HEX-HRU system. The numerical study employs the following assumptions to establish control equations that describe the mass and energy transfer within the system:

(1) A local thermal equilibrium exists between the TCES composite materials and the airflow in the reaction bed [8,45].
(2) The radiative heat transfer in the TCES reactor and HRU is disregarded [57,58].
(3) The airflow is considered as an ideal gas and is assumed to be uniformly distributed, following Darcy's law in the reaction bed [59].
(4) The TCES composite materials are uniformly dispersed throughout the reaction bed. Additionally, the impact of the sieve plate located at the base of the reaction bed on the solid-gas reaction is disregarded [24].

3.1. Reaction kinetics

The kinetics of the reaction associated with salt hydrates can be described using three key parameters: the time-dependent extent of conversion, pressure, and temperature [57]. The rate of conversion of salt hydrates during the charging and discharging processes is expressed as:

$$\frac{\partial \alpha}{\partial t} = R_{kin}\alpha\left(1-\frac{P_v}{P_{eq}}\right) = A_{freq}exp\left(-\frac{E_a}{RT}\right)\alpha\left(1-\frac{P_v}{P_{eq}}\right) \quad \text{for discharging} \tag{2}$$

where α is the conversion degree; R_{kin} is the chemical kinetic factor, s^{-1}; P_v and P_{eq} are the partial pressure of water vapor and the equilibrium pressure of water vapor, respectively, Pa; A_{freq} is the pre-exponential Arrhenius factor, s^{-1}; R is universal gas constant, $J{\cdot}mol^{-1}{\cdot}K^{-1}$, and E_a refers to the Arrhenius activation energy, $J{\cdot}mol^{-1}$.

The conversion degree of salt hydrate can be defined as:

$$\alpha(t) = \frac{m_{s,i} - m_s(t)}{m_{s,i} - m_{s,f}} \tag{3}$$

where $m_{s,i}$ and $m_{s,f}$ are respectively the initial and final mass of the salt hydrate (i.e., $CaCl_2{\cdot}6H_2O$) in the reaction bed, kg. Given that the utilized model in COMSOL exclusively considers concentration, the expression for the degree of conversion has been accordingly modified to:

$$\alpha(t) = \frac{c_{s,i} - c_s(t)}{c_{s,i} - c_{s,f}} \tag{4}$$

where $c_{s,i}$ and $c_{s,f}$ are the initial and final molar concentration of the salt hydrate, $mol{\cdot}m^{-3}$, respectively.

Assuming that the mass transfer and chemical reaction processes occur rapidly enough during the solid-gas reaction to maintain the system at the prevailing temperature, the equilibrium pressure (P_{eq}) and temperature (T) can be correlated using the Clausius-Clapeyron equation, which is given by:

$$ln\left(\frac{P_{eq}}{P_{ref}}\right) = -\frac{\Delta H_r}{RT_{ref}} + \frac{\Delta S_r}{R} \tag{5}$$

where P_{ref} is the reference pressure, Pa; ΔH_r is the reaction enthalpy, $J{\cdot}mol^{-1}$; T_{ref} is the reference temperature, K; and ΔS_r is the reaction entropy, $J{\cdot}mol^{-1}{\cdot}K^{-1}$.

3.2. Mass conservation

Given the absence of mass transfer between the reactor and the external environment, the density of the salt hydrate decreases during the charging process, while the densities of the dehydrated salt and water vapor increase. The mass transfer equation for water vapor can be expressed as follows:

$$\varepsilon\frac{\partial \rho_v}{\partial t} = S_w - \nabla(\rho_v \vec{u}) + D_g\Delta\rho_v \tag{6}$$

where ε is the porosity of the TCES composite materials; ρ_v is the density of water vapor, $kg{\cdot}m^{-3}$; $\vec{u}$ is the velocity vector, $m{\cdot}s^{-1}$; D_g is the diffusion coefficient of water vapor in the reaction bed, $m^2{\cdot}s^{-1}$; and S_w is the mass source and is expressed as:

$$S_w = zc_{s,i}\frac{\partial \alpha}{\partial t}M_v \tag{7}$$

where z is the stoichiometric number of the reaction; and M_v is the molecular mass of vapor, $kg{\cdot}mol^{-1}$.

Furthermore, the mass conservation equation for the moist air mixture can be determined as:

$$\varepsilon\frac{\partial \rho_a}{\partial t} = S_w - \nabla(\rho_a \vec{u}) \tag{8}$$

where ρ_a is the density of the airflow (i.e., moist air mixture), $kg{\cdot}m^{-3}$.

3.3. Mass transport

The flow of moist air mixture through the reaction bed follows the Brinkman-Forchheimer extended Darcy model, and the corresponding equation for mass transport is expressed as follows:

$$\frac{\rho_a}{\varepsilon}\frac{\partial \vec{u}}{\partial t} + \frac{\rho_a \vec{u}\nabla\vec{u}}{\varepsilon^2} = \nabla\left[-\vec{P_a}\mathrm{I} + \frac{\mu}{\varepsilon}\left(\nabla\vec{u} + (\nabla\vec{u})^T - \frac{2\mu}{3\varepsilon}(\nabla\vec{u})\mathrm{I}\right)\right] + S_w\frac{\vec{u}}{\varepsilon^2} - \frac{\mu}{k}\vec{u} \tag{9}$$

where k is the permeability of the TCES composite materials in the reaction bed, m^2; and μ is the dynamic viscosity of the moist air mixture, Pa·s.

3.4. Energy conservation

In the TCES reactor, the energy balance equation of the reaction bed is explicated as:

$$(1-\varepsilon)\rho_s C_s\frac{\partial T}{\partial t} = \nabla\left(\lambda_{eff}\nabla T\right) - C_a\rho_a\vec{u}\nabla T + h_{a,Al}(T_{Al} - T) + \dot{q} \tag{10}$$

where ρ_s is the density of the salt, $kg{\cdot}m^{-3}$; C_s and C_a are the specific heat of the salt and water vapor, $J{\cdot}g^{-1}{\cdot}K^{-1}$; λ_{eff} is the effective thermal conductivity of the reaction bed, $W{\cdot}m^{-1}{\cdot}K^{-1}$; T_w is the temperature of the water in water channels, K; $h_{a,Al}$ is the convective heat transfer coefficient between the air flow and aluminium water channels, $W{\cdot}m^{-2}{\cdot}K^{-1}$; and $\dot{q}$ is the heat absorbed or released by the salt hydrate in the charging or discharging process, $W{\cdot}m^{-3}$.

The effective thermal conductivity of the reaction bed can be

described as follows:

$$\lambda_{\text{eff}} = (1-\varepsilon)\lambda_{\text{s}} + \varepsilon\lambda_{\text{a}} \tag{11}$$

where λ_{s} and λ_{a} represent the thermal conductivities of the solid salt and airflow, respectively, $\text{W}\cdot\text{m}^{-1}\cdot\text{K}^{-1}$.

The convective heat transfer coefficient between the airflow and aluminium water channels is described as [60]:

$$h_{\text{a,Al}} = Nu\frac{\lambda_{\text{a}}}{d_{\text{int}}/2} = 0.023Re^{0.8}Pr^{0.4}\frac{\lambda_{\text{a}}}{d_{\text{int}}/2} \tag{12}$$

where d is the distance between the adjacent water channels, m; Re is the Reynolds number; and Pr is the Prandtl number.

The heat absorbed or released by the thermochemical reaction of salt hydrate is described as:

$$\dot{q} = \pm zc_{\text{s,i}}\frac{\partial\alpha}{\partial t}\Delta H_{\text{r}} \tag{13}$$

where "−" is for the charging process and "+" is for the discharging process.

The energy balance equation of the aluminium water channels is expressed as:

$$\rho_{\text{Al}}C_{\text{Al}}\frac{\partial T_{\text{Al}}}{\partial t} = \lambda_{\text{Al}}\nabla^2 T_{\text{Al}} + h_{\text{a,Al}}(T_{\text{Al}} - T) + h_{\text{Al,w}}(T_{\text{w}} - T_{\text{Al}}) \tag{14}$$

where ρ_{Al}, C_{Al}, and λ_{Al} are the density, specific heat capacity, and thermal conductivity of the aluminium water channels, $\text{kg}\cdot\text{m}^{-3}$, $\text{J}\cdot\text{g}^{-1}\cdot\text{K}^{-1}$, and $\text{W}\cdot\text{m}^{-1}\cdot\text{K}^{-1}$, respectively; and $h_{\text{Al,w}}$ is the convective heat transfer coefficient between the aluminium water channels and waterflow, it is calculated from Nusselt number.

The energy balance equation of water in the water channel is expressed as:

$$\rho_{\text{w}}C_{\text{w}}\frac{\partial T_{\text{w}}}{\partial t} + \rho_{\text{w}}C_{\text{w}}\vec{u}_{\text{w}}\nabla T_{\text{w}} = \lambda_{\text{w}}\nabla^2 T_{\text{w}} + h_{\text{Al,w}}(T_{\text{Al}} - T_{\text{w}}) \tag{15}$$

where ρ_{w}, C_{w}, and λ_{w} are the density, specific heat capacity, and thermal conductivity of the waterflow in the water channel, $\text{kg}\cdot\text{m}^{-3}$, $\text{J}\cdot\text{g}^{-1}\cdot\text{K}^{-1}$, and $\text{W}\cdot\text{m}^{-1}\cdot\text{K}^{-1}$, respectively; and $\vec{u}_{\text{w}}$ is the velocity of waterflow, $\text{m}\cdot\text{s}^{-1}$.

3.5. Boundaries and initial conditions

Given that the TCES reactor is typically located in the indoor environment with negligible local wind speeds, natural convective heat exchange is the predominant mode of heat transfer between the reactor and its surroundings. Consequently, the heat balance equation for the external surface of the TCES reactor can be expressed as follows:

$$-\mathbf{n}(\lambda_{\text{ins}}\nabla T) = h_{\text{ins}}(T_{\text{amb}} - T) \tag{16}$$

where λ_{ins} is the thermal conductivity of the insulating material, $\text{W}\cdot\text{m}^{-1}\cdot\text{K}^{-1}$; h_{ins} is the natural convective heat transfer coefficient between the reactor and ambient air, $\text{W}\cdot\text{m}^{-2}\cdot\text{K}^{-1}$; and T_{amb} is the ambient air temperature, K.

At the initial stage, the temperature T, pressure P, degree of conversion α, air velocity $\vec{u}$, and water velocity $\vec{u}_{\text{w}}$ at any location within the reactor are assumed to be uniform.

$$T = T_0; P = P_{\text{ref}}; \alpha = 1; \vec{u} = 0; \vec{u}_{\text{w}} = 0 \tag{17}$$

The air and water variables exhibit constancy at the system and HEX inlet. Non-slip boundary conditions have been imposed on the reactor and the HEX walls.

As this TCES system is an open system, the pressure inside the reactor is equivalent to the ambient pressure P_{ref}. The temperature gradient at the system outlet (i.e., HRU air outlet) and HEX water outlet are zero. Furthermore, the mass flow through the outlet boundary is assumed to be convectively dominated; therefore, any mass flow through this boundary due to diffusion is considered negligible.

3.6. Performance metrics

In this study, the system's overall thermal efficiency during the discharging process can be defined as the amount of heat absorbed by the airflow or the amount of heat absorbed by the waterflow divided by the amount of heat released from the thermochemical reaction of the TCES composite materials, which can be expressed as:

$$\eta_{\text{th}} = \frac{Q_{\text{ab,a}}}{Q_{\text{re}}} \text{ or } \eta_{\text{th}} = \frac{Q_{\text{ab,w}}}{Q_{\text{re}}} \tag{18}$$

where $Q_{\text{ab,a}}$ and $Q_{\text{ab,w}}$ is the amount of heat absorbed by the airflow and waterflow, respectively, kJ; and Q_{re} is the amount of heat released from the TCES composite materials.

The amount of heat absorbed by the airflow is given as:

$$Q_{\text{ab,a}} = \int C_{\text{a}}\dot{m}_{\text{a}}(T_{\text{a,out}} - T_{\text{a,in}})dt \tag{19}$$

where $\dot{m}_{\text{a}}$ is the mass flow rate of the airflow, $\text{kg}\cdot\text{s}^{-1}$; $T_{\text{a,out}}$ and $T_{\text{a,in}}$ are the airflow temperatures at the inlet and outlet of the reactor, respectively, K.

The amount of heat absorbed by the waterflow is given as:

$$Q_{\text{ab,w}} = \int C_{\text{w}}\dot{m}_{\text{w}}(T_{\text{w,out}} - T_{\text{w,in}})dt \tag{20}$$

where $\dot{m}_{\text{w}}$ is the mass flow rate of the waterflow, $\text{kg}\cdot\text{s}^{-1}$; $T_{\text{w,out}}$ and $T_{\text{w,in}}$ are the waterflow temperatures at the inlet and outlet of the water channel, respectively, K.

The amount of heat released by the TCES composite materials is given as:

$$Q_{\text{re}} = \int\int zc_{\text{s,i}}\frac{\partial\alpha}{\partial t}\Delta H_{\text{r}}dtdV \tag{21}$$

Table 3 lists some key parameters of the combined TCES reaction bed and HEX unit and their respective values used in this numerical study.

4. Model validation

To validate the established mathematical model in this study, an experimental setup of a combined TCES reaction bed with an embedded HEX unit was built for the discharging process. Fig. 4 present the picture of the combined TCES reaction bed with HEX. The reaction bed was constructed using a 1 mm-thick metal mesh, with dimensions of 0.282 m × 0.282 m × 0.050 m (length × width × height). Within the reaction bed, three aluminium water channels, each of 0.002 m in thickness, were incorporated. Water was used as the heat exchange medium within HEX, while the remaining space in the reaction bed was filled with TCES composite materials. In order to compare the simulation results with the experimental measurements, the root mean square deviation (*RMSD*) is defined by the following equation: [54].

$$RMSD = \sqrt{\frac{\sum\left[\left(x_{\text{sim,i}} - x_{exp,\text{i}}\right)/x_{exp,\text{i}}\right]^2}{n}} \tag{22}$$

The simulated and experimental results of the reactor outlet airflow temperature and HEX outlet waterflow temperature are shown in Fig. 5 (a) and (b), respectively. Both simulated and experimental reactor outlet air temperatures rapidly increased during the initial stage, reaching their respective peak values of 34.54 °C and 34.6 °C. Then, both temperature curves decreased until the end. The maximum difference between simulated and experimental reactor outlet air temperatures was 2.9 °C during the initial stage. The simulated and experimental HEX outlet water temperature followed a similar trend to the reactor outlet

Table 3
Key parameters of the combined TCES reaction bed and HEX unit.

Parameters	Description	Value
M_v	Molecular mass of vapor ($g{\cdot}mol^{-1}$)	18.02
M_s	Molecular mass of salt ($g{\cdot}mol^{-1}$)	219.08
$c_{s,i}$	Molar concentration ($mol{\cdot}m^{-3}$)	1660
k	Permeability of TCES composite materials (m^2)	$8.24{\cdot}10^{-6}$
C_s	Specific heat of the TCES composite materials ($J{\cdot}g^{-1}{\cdot}K^{-1}$)	0.626
λ_s	Thermal conductivity of TCES composite materials ($W{\cdot}m^{-1}{\cdot}K^{-1}$)	0.0669
ε	Porosity	0.64
E_a	Activation energy ($J{\cdot}mol^{-1}$)	44,700 [61]
ΔH_r	Reaction enthalpy ($J{\cdot}mol^{-1}$)	53,400 [62]
ΔS_r	Reaction entropy ($J{\cdot}mol^{-1}{\cdot}K^{-1}$)	104.62 [63]
D_g	Gas diffusion coefficient ($m^2{\cdot}s^{-1}$)	$2.3{\cdot}10^{-8}$
C_a	Specific heat of the airflow ($J{\cdot}g^{-1}{\cdot}K^{-1}$)	1.006
R	Universal gas constant ($J{\cdot}mol^{-1}{\cdot}K^{-1}$)	8.314
P_{ref}	Reference pressure (Pa)	101,325
C_{Al}	Specific heat of the aluminium water channels ($J{\cdot}g^{-1}{\cdot}K^{-1}$)	0.897
ρ_{Al}	Density of the aluminium water channels ($kg{\cdot}m^{-3}$)	2700
λ_{Al}	Thermal conductivity of the aluminium water channels ($W{\cdot}m^{-1}{\cdot}K^{-1}$)	209
C_w	Specific heat of the water ($J{\cdot}g^{-1}{\cdot}K^{-1}$)	4.184
ρ_w	Density of the water ($kg{\cdot}m^{-3}$)	1000
$T_{in,a}$	Airflow temperature at system inlet (°C)	20
$T_{in,w}$	Waterflow temperature at HEX inlet (°C)	27
λ_{ins}	Thermal conductivity of the insulating material ($W{\cdot}m^{-1}{\cdot}K^{-1}$)	0.035
L	Length of the reaction bed (m)	0.280
W	Width of the reaction bed (m)	0.280
H	Height of the reaction bed (m)	0.05
l	Length of the HEX waterflow channel (m)	0.28
w	Width of the HEX waterflow channel (m)	0.002
h	Height of the HEX waterflow channel (m)	0.05
d_{int}	Interval of the HEX waterflow channel (m)	0.0262

Note: k, C_s, λ_s, ε and D_g of the vermiculite-$CaCl_2$ composite in this study are sourced from self-conducted experimental tests.

air temperature, peaking at 28.52 °C and 28.49 °C, respectively. The maximum difference between simulated and experimental HEX outlet water temperatures was 0.67 °C. According to Eq. (22), the *RMSD* values of the reactor outlet air temperature and HEX outlet water temperature were 1.86 % and 0.54 %, respectively. The comparison indicates that the simulation results obtained using the proposed mathematical model agree well with the experimental data. Therefore, the mathematical model developed in Section 3 can accurately predict the performance of the proposed TCES-HEX-HRU system during the discharging process.

5. Results and discussion

Based on the mathematical model established in Section 3, a numerical analysis of the thermal performance of the TCES-HEX-HRU system during the discharging process is conducted, and comparisons are made with a typical TCES system without the involvement of the HEX and HRU (i.e., the TCES-only system) and another TCES system with the HEX but without the HRU (i.e., the TCES-HEX system).

5.1. Effect of the internal heat exchange and external heat recovery schemes

The thermal performance of the TCES-HEX-HEX system over a complete discharging process is investigated and compared with the TCES-only and TCES-HEX systems. Although evaluating the performance of the TCES system under winter conditions and accurately predicting its real-world capabilities can be achieved by considering a low system inlet airflow temperature or a temperature close to the outdoor winter condition, it is essential to strike a balance among various factors when selecting the inlet airflow temperature for the TCES system. A low inlet airflow temperature may result in a slow conversion rate and a low heat release rate due to the low-level moisture saturation of the cold air, which consequently affects the performance and efficiency of the TCES system. Directly introducing cold air into the TCES system is impractical at present. Instead, preheating the air to ensure it has the capacity to carry more moisture before entering the TCES system is necessary. In this numerical study, it is assumed that the airflow has

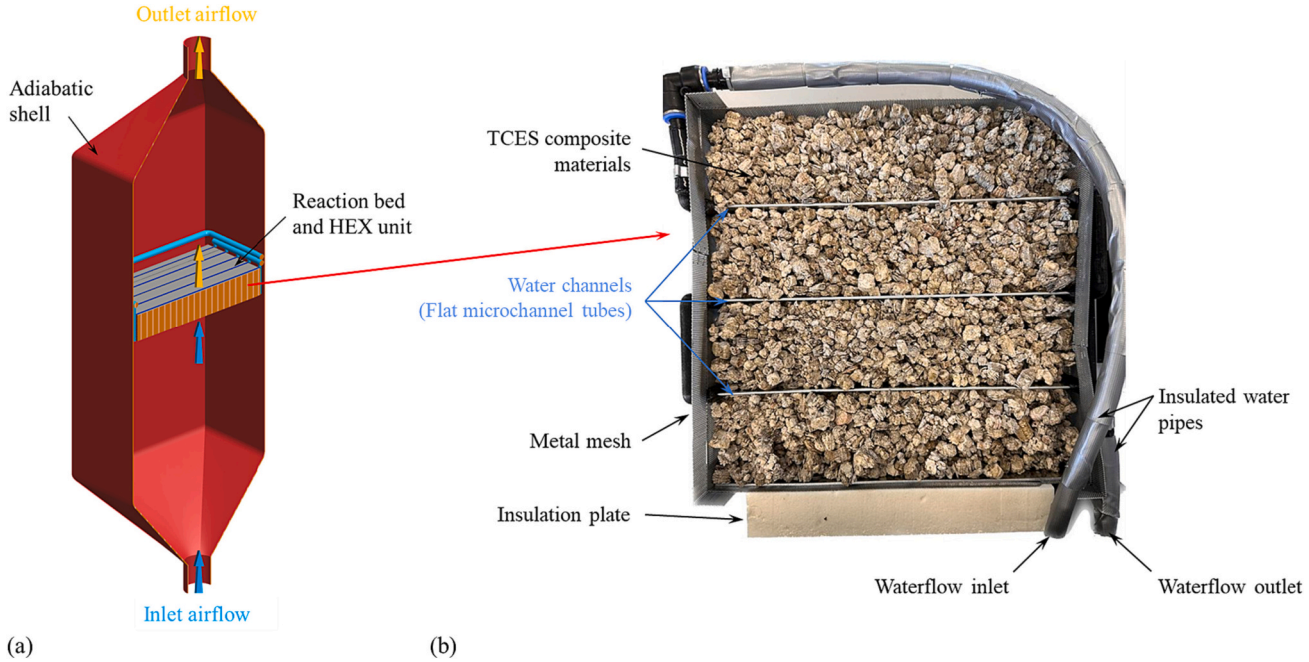

Fig. 4. (a) Schematic diagram of the reactor in experiment; and (b) Top view of the experimental set-up of the combined TCES reaction bed and HEX unit.

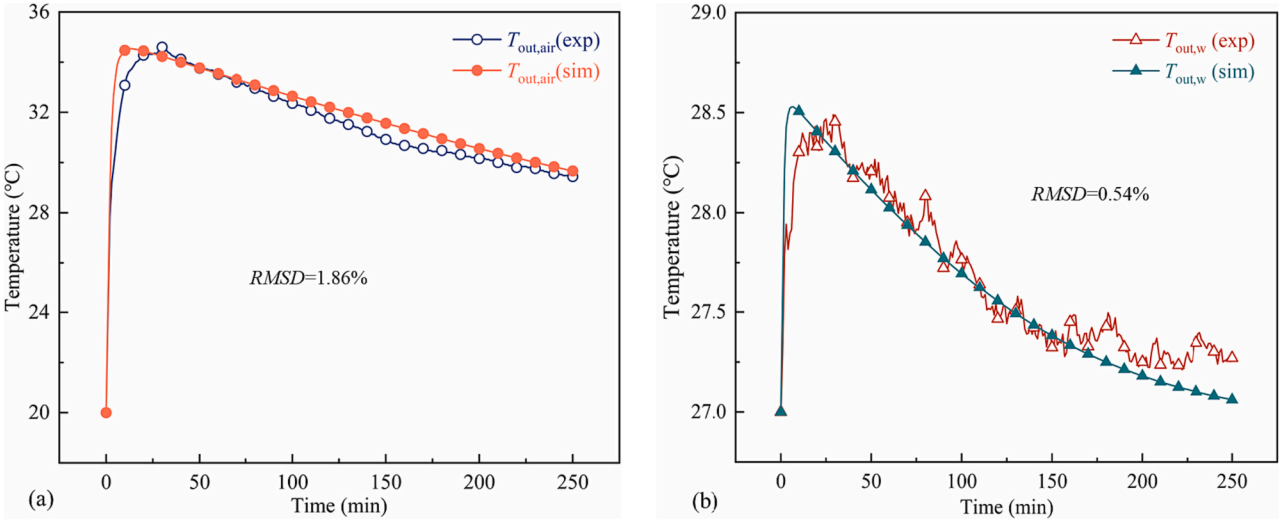

Fig. 5. Simulation and experiment results of (a) reactor outlet airflow temperature and (b) HEX outlet waterflow temperature.

been preheated and humidified to 21 °C and 80 % relative humidity (RH) before entering the system. The mass flow rate of the airflow is 0.014 kg·s^{-1}. The HEX inlet waterflow temperature of is 27 °C, with a mass flow rate of 0.01 kg·s^{-1}. Fig. 6(a) depicts the reactor outlet airflow temperature for the TCES-only, TCES-HEX and TCES-HEX-HRU systems. The peak airflow temperature at the reactor outlet of the TCES-only system is the highest among the three, measuring 42.52 °C. It is 4.56 °C higher than that of the TCES-HEX system, in which a portion of the heat released during the salt hydration process is transferred to the water inside the water channels. After that, the reactor outlet temperature of the TCES-HEX system exceeds that of the TCES-only system at around 126th minute as the temperatures decrease. This phenomenon is attributed to the decline in heat generation from the salt hydration reaction as the discharging process progresses. As the salt near the bottom of the reaction bed reaches a state of complete or near-complete reaction, its localized temperature falls below that of the water flow circulating through the channels. Consequently, the heat transfer mechanism causes the water flow to transfer thermal energy to the airflow within the reaction bed, thereby sustaining a higher temperature in the latter. The reactor outlet airflow temperature of the TCES-HEX-HRU system is only 0.41 °C lower than that of the TCES-only system at the initial stage, however it is higher than both TCES-only and TCES-HEX systems in the subsequent stages. This indicates that the incorporation of HRU contribute to achieving effective heat recovery during the discharging process. This is also reflected in the outlet waterflow temperature of HEX, as shown in Fig. 6(b). Throughout the entire discharging process, the HEX outlet waterflow temperature of the TCES-HEX-HRU system remains higher than that of the TCES-HEX system. The involvement of HRU results in a maximum increase of 2.65 °C and an average increase of 2.1 °C in the HEX outlet water temperature.

According to Eq. (18), the total thermal efficiencies of the three systems are calculated and presented in Table 4. The TCES-only system exhibits the highest system's overall thermal efficiency among these three systems at 97.79 %, as the heat generated by the salt in the hydration reaction in this system is directly transferred to the airflow which serves as the heat transfer medium, with only a small portion of

Table 4
Discharging performance of the TCES-only, TCES-HEX and TCES-HEX-HRU.

System type	Peak $T_{out,a}$ (°C)	Peak $T_{out,w}$ (°C)	Q_{ab} (kJ)	η_{th} (%)
TCES-only	42.52	–	2555.40	97.79
TCES-HEX	37.95	29.15	307.34	12.67
TCES-HEX-HRU	42.11	31.77	1998.16	82.35

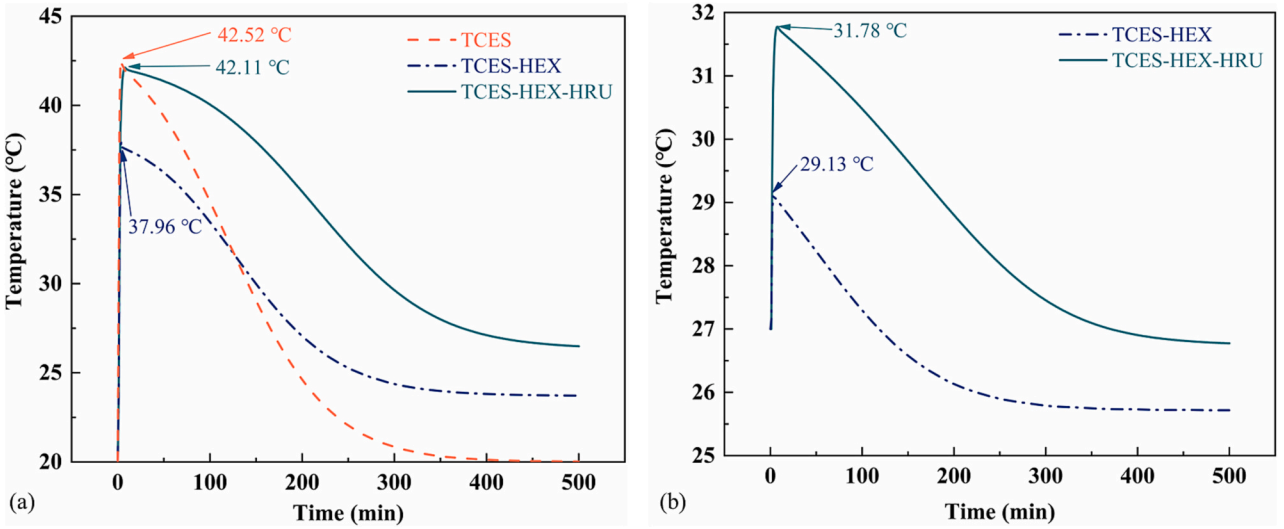

Fig. 6. Variation of (a) reactor outlet airflow temperatures, and (b) HEX outlet waterflow temperatures over a complete discharging process.

heat dissipated to the surroundings through insulation materials. However, in the other two water-based systems, only a portion of the heat is absorbed by the water (i.e., the target heated medium), while the remaining heat is absorbed by the air and released to the surroundings to some extents. Nevertheless, the incorporation of HRU in the TCES-HEX-HRU system allows for the recovery of some waste heat from the exhausted air stream, resulting in a significantly higher system's overall thermal efficiency of approximately 82.35 %, which is approximately 69 percentage points higher than that of the TCES-HEX system. Although the system's overall thermal efficiency of the TCES-only system is higher than that of the TCES-HEX-HRU system, there are practical challenges associated with the installation of extensive piping for the air-based TCES-only system in existing buildings. Additionally, the air-based TCES-only system lacks the capability to easily regulate the real-time outlet temperature. In contrast, the water-based TCES-HEX-HRU system can be directly integrated to the existing centralized heating systems in buildings, addressing the aforementioned challenges in the TCES-only system. Furthermore, with the inclusion of HRU, the penalty in the system's overall thermal efficiency due to the increased heat transfer resistance inside the reactor bed becomes marginal, resulting in a system's overall thermal efficiency that reaches an acceptable level.

5.2. Coupling effect of system inlet airflow and HEX inlet waterflow temperatures

The system inlet airflow temperature and HEX inlet waterflow temperature are two key factors determining the performance of the TCES-HEX-HRU system during the discharging process. Therefore, in this section, the influence of the system inlet airflow temperature and HEX inlet waterflow temperature on the maximum temperature lift and system's overall thermal efficiency of the TCES-HEX-HRU system is assessed. The system inlet airflow temperature is assumed to vary within the range of 15 °C to 24 °C, while the HEX inlet water temperature ranges from 25 °C to 30 °C. The mass flow rates of the system inlet airflow and HEX inlet waterflow are specified as 0.014 $kg{\cdot}s^{-1}$and 0.01 $kg{\cdot}s^{-1}$, respectively.

The effect of the system inlet airflow temperature and HEX inlet waterflow temperature on the HEX maximum temperature lift is illustrated in Fig. 7(a). The HEX maximum temperature lift increases with the higher system inlet airflow temperature. This can be attributed to the reduced temperature difference between the TCES composite materials and the airflow as the system inlet airflow temperature rises. Consequently, the heat transferred from the TCES composite materials to the airflow decreases while the heat transferred to the waterflow increases. Specifically, when the HEX inlet waterflow temperature is maintained at 25 °C, the HEX maximum temperature lift reaches 4.91 °C at an inlet airflow temperature of 15 °C, and it increases to 5.15 °C at a system inlet airflow temperature of 24 °C. However, the influence of the HEX inlet waterflow temperature on the HEX maximum temperature lift is opposite to that of the system inlet airflow temperature. The HEX maximum temperature lift decreases as the HEX inlet waterflow temperature increases. This can be caused by the decrease in temperature difference between the TCES composite materials and the waterflow as the HEX inlet water temperature rises. As a result, there is a reduction in the heat transferred from the TCES composite materials to the waterflow while the heat transferred to the airflow increases. When the system inlet airflow temperature is set at 15 °C and the HEX inlet waterflow temperature is set at 25 °C, the HEX maximum temperature lift is only 4.08 °C.

Fig. 7(b) depicts the influence of the system inlet airflow temperature and HEX inlet waterflow temperature on the system's overall thermal efficiency. Consistent with the impact on the maximum temperature lift, an increase in the system inlet airflow temperature leads to an improvement in the system's overall thermal efficiency, while an increase in the HEX inlet waterflow temperature results in a decrease in the system's overall thermal efficiency. Specifically, when the HEX inlet waterflow temperature is maintained at 25 °C, the system achieves a system's overall thermal efficiency of 75.77 % at a system inlet airflow temperature of 15 °C. The system's overall thermal efficiency increases to 80 % as the system inlet airflow temperature rises to 17.8 °C. Moreover, with further increases in the system inlet airflow temperature, the system's overall thermal efficiency reaches 90 % and 92.12 % at system inlet airflow temperatures of 23.4 °C and 24 °C, respectively. Conversely, as the HEX inlet waterflow temperature increases, the system's overall thermal efficiency declines. When the HEX inlet waterflow temperature reaches 30 °C, it becomes extremely difficult for the system's overall thermal efficiency to exceed 80 % within the specified range of the system inlet airflow temperatures.

5.3. Coupling effect of airflow and waterflow mass flow rates

The mass flow rate of airflow and the mass flow rate of waterflow are also crucial operational parameters that impact the system discharging performance. This section discusses the combined effects of these two parameters on the HEX maximum temperature lift and system's overall thermal efficiency. Assuming the system inlet airflow temperature and HEX inlet waterflow temperature are set at 21 °C and 27 °C, respectively, the mass flow rate of waterflow ranges from 0.0025 $kg{\cdot}s^{-1}$ to 0.025 $kg{\cdot}s^{-1}$, while the mass flow rate of airflow varies between 0.009 $kg{\cdot}s^{-1}$ and 0.017 $kg{\cdot}s^{-1}$. Fig. 8(a) shows the influence of the mass flow rate of airflow and the mass flow rate of waterflow on the HEX maximum temperature lift. When the mass flow rate of the waterflow remains

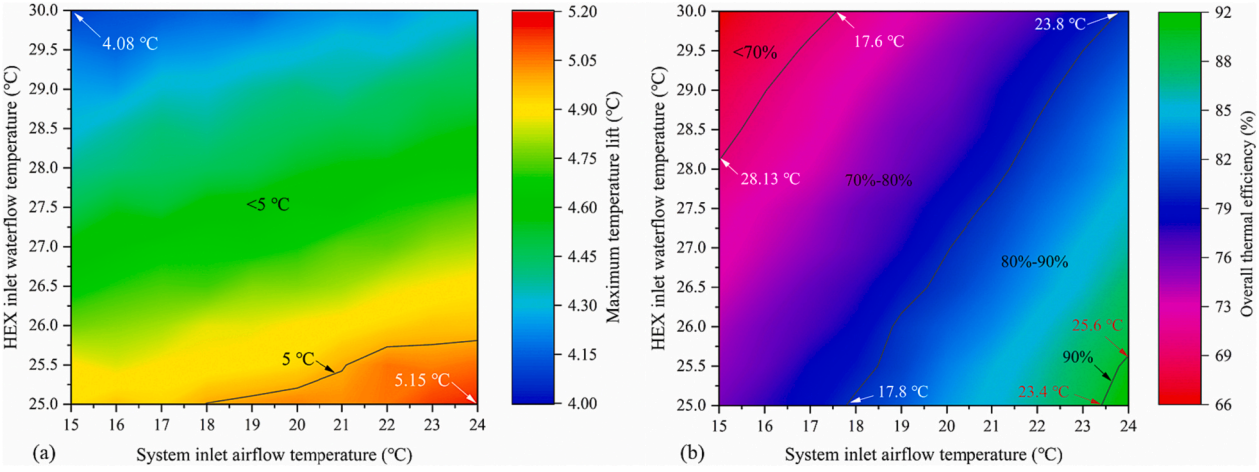

Fig. 7. Effect of system airflow inlet temperature and HEX water inlet temperature on (a) HEX maximum temperature lift, and (b) system's overall thermal efficiency.

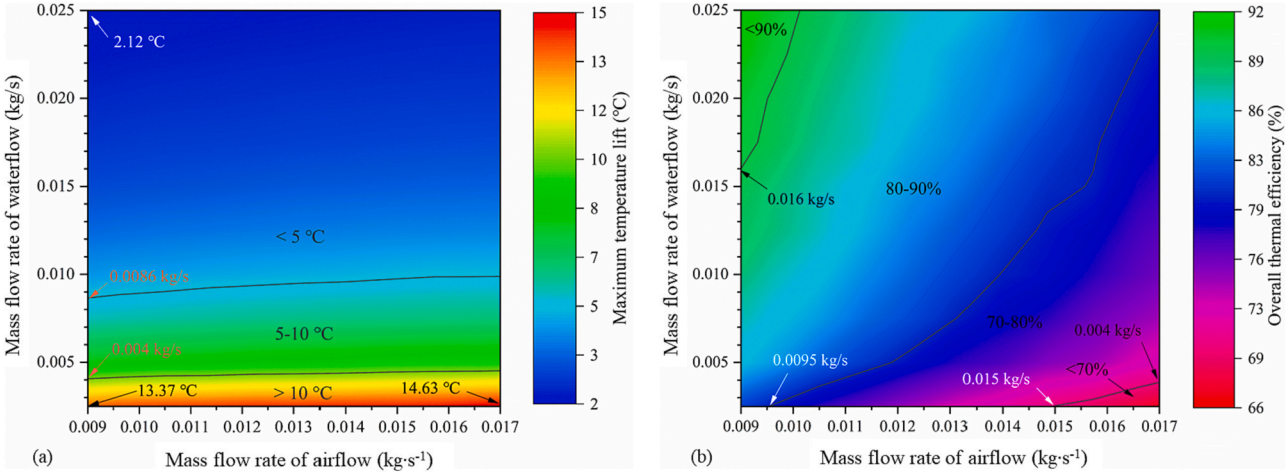

Fig. 8. The effect of mass flow rate of airflow and the mass flow rate of waterflow on (a) HEX maximum temperature lift, and (b) system's overall thermal efficiency.

constant, the maximum temperature lift in HEX slightly increases with an augmentation in the mass flow rate of the airflow, owing to the enhanced heat and mass transfer within the reaction bed. Specifically, when the mass flow rate of waterflow in HEX is maintained at 0.0025 kg·s^{-1}, the HEX maximum temperature lift is 13.37 °C at a mass flow rate of airflow of 0.009 kg·s^{-1}. However, increasing the mass flow rate airflow to 0.017 kg·s^{-1} results in a mere increment of 1.26 °C, reaching 14.63 °C.

In contrast to the effect of the mass flow rate of airflow, the HEX maximum temperature lift experiences a significant decline with an increase in the mass flow rate of waterflow starting from 0.0025 kg·s^{-1}, followed by a diminishing rate of decrease until reaching a steady state. This is because the increase in the mass flow rate of waterflow causes a reduced residence time of the unit mass of water within the water channels, leading to a decrease in the amount of heat obtained. For instance, when the mass flow rate of waterflow increases from 0.0025 kg·s^{-1} to 0.004 kg·s^{-1}, the HEX maximum temperature lift decreases by 3.37 °C. However, when the mass flow rate of waterflow in HEX further increases from 0.0086 kg·s^{-1} to 0.025 kg·s^{-1}, the HEX maximum temperature lift only diminishes by 2.88 °C. It can be observed from the provided data and Fig. 8(a) that the mass flow rate of waterflow has a significant impact on the HEX maximum temperature lift, while the effect of the mass flow rate of airflow on the HEX maximum temperature lift is negligible.

Fig. 8(b) portrays the influence of the mass flow rate of airflow and the mass flow rate of waterflow on the system's overall thermal efficiency. Notably, an increase in the mass flow rate of airflow corresponds to a decrease in system's overall thermal efficiency. This is because, with the increase in the mass flow rate of airflow, more heat is carried away from the reaction bed by the airflow rather than the waterflow. While the effect of the increase in the mass flow rate of waterflow yields an opposing outcome, resulting in an elevation of the system's overall thermal efficiency. This is because, with the increase in the mass flow rate of waterflow, more heat is absorbed by the waterflow and transferred to the central heating system rather than the airflow. Under the condition of a constant mass flow rate of waterflow of 0.0025 kg·s^{-1}, the system's overall thermal efficiency achieves 80 % when the mass flow rate of airflow reaches 0.0095 kg·s^{-1}. Subsequently, as the mass flow rate of airflow progressively rises, the system's overall thermal efficiency exhibits a gradual decline, ultimately reaching 70 % when the mass flow rate of airflow reaches 0.015 kg·s^{-1}. Conversely, when maintaining the mass flow rate of airflow at a steady value of 0.009 kg·s^{-1} and commencing with a mass flow rate of waterflow of 0.0025 kg·s^{-1}, the system's overall thermal efficiency already surpasses 80 %. Moreover, with a further increase in the mass flow rate of waterflow to 0.016 kg·s^{-1}, the system's overall thermal efficiency attains 90 %.

The results indicate that the mass flow rate of airflow and the mass flow rate of waterflow exert contrasting influences on both the maximum temperature lift and system's overall thermal efficiency. Consequently, it becomes imperative to strike a judicious balance between the maximum temperature lift and system's overall thermal efficiency when determining the appropriate values for the mass flow rate of airflow and the mass flow rate of waterflow, thereby identifying the optimal velocity range. Remarkably, when the mass flow rate of airflow remains below 0.0095 kg·s^{-1} within the presumed range of mass flow rate of waterflow, the system achieves a system's overall thermal efficiency surpassing 80 %. Similarly, when the mass flow rate of waterflow remains below 0.004 kg·s^{-1}, the maximum temperature lift in HEX exceeds 10 °C. Based on the provided data, it can be inferred that for achieving favourable performance in terms of both HEX maximum temperature lift and system's overall thermal efficiency, it is advisable to maintain the mass flow rate of airflow below 0.0095 kg·s^{-1} and the mass flow rate of waterflow below 0.004 kg·s^{-1}.

5.4. *Effect of the number of water channels*

The number of water channels denoted as "*n*" in the HEX, is a crucial structural parameter that significantly affects the performance of the

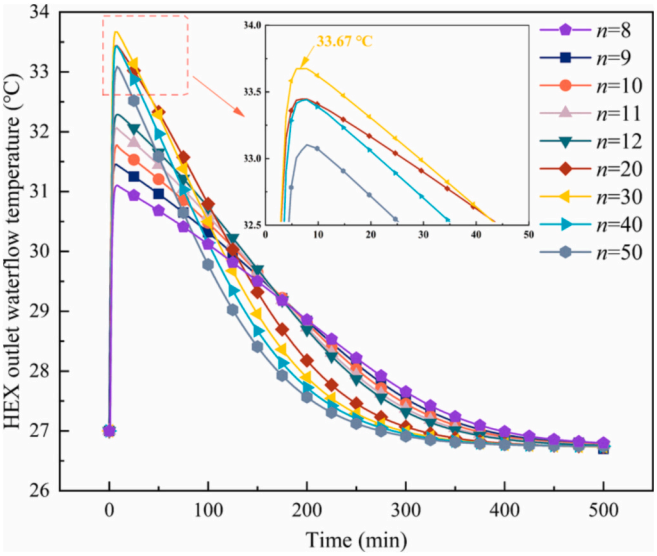

Fig. 9. The effect of the number of water channels on the HEX outlet waterflow temperature.

TCES-HEX-HRU system. This section investigates the impact of the number of water channels in the HEX on the discharging process while maintaining constant reactor volume and inlet parameters. As shown in Fig. 9, the highest temperature of HEX outlet waterflow increases with an increase in the number of water channels within HEX, when the number of water channels do not exceed 30. Specifically, when $n = 8$ (the volume of TCES composite material in reaction bed $V_s = 3.64$ L), the recorded highest temperature of HEX outlet waterflow is 31.10 °C. However, as the number of water channels increases to 30 (i.e., Vs = 3.08 L), the highest temperature of HEX outlet waterflow rises by 2.57 °C, reaching 33.67 °C. When the number of water channels exceeds 30, an increase in the number of water channels leads to a decrease in the highest temperature of HEX outlet waterflow. For instance, when the number of water channels increases from 30 to 55 (V_s: 3.08 L → 2.25 L), the highest temperature of HEX outlet waterflow decreases from 33.67 °C to 33.02 °C.

Fig. 10 illustrates the impact of the number of water channels on the heat release from the TCES composite materials. As the number of water channels increases in HEX, there is a decrease in the amount of heat released by the TCES composite materials during the discharge process. The relationship between the number of water channels and the amount of heat absorbed by the waterflow is also depicted in Fig. 10. Initially, the amount of heat absorbed by the waterflow increases with an increase in the number of water channels, reaching a maximum value of 2067.23 kJ when $n = 15$ (note: the value is 2063.07 kJ and 2061.06 kJ when n is 14 and 16, respectively). However, as the number of water channels continues to increase, the amount of heat absorbed by the waterflow decreases. This is because the amount of heat absorbed by the waterflow is influenced by the amount of heat released by the TCES composite materials and the heat transfer efficiency. Although increasing the number of water channels reduces the amount of heat released by the TCES composite materials during the discharge process, the increased contact area between the water channels and TCES composite materials enhances the heat transfer efficiency. When the number of water channels is below 15 (i.e., $V_s > 3.5$ L), the positive effect of increased heat transfer efficiency outweighs the decrease in heat released by TCES composite materials. However, the opposite effect occurs when the number of water channels exceeds 15 (i.e., $V_s < 3.5$ L). Furthermore, Fig. 10 also presents the relationship between the system's overall thermal efficiency of the system and the number of water channels in the HEX. The system's overall thermal efficiency exhibits a significant improvement as the number of water channels increases within the range of 10 to 25. With a further increase in the number of water channels, the system's overall thermal efficiency of the system reaches a plateau and gradually increases until it reaches its highest value of 92.09 % at $n = 35$ (i.e., $V_s = 2.38$ L). Subsequently, as the number of water channels continues to increase, the system's overall thermal efficiency of the system starts to decline.

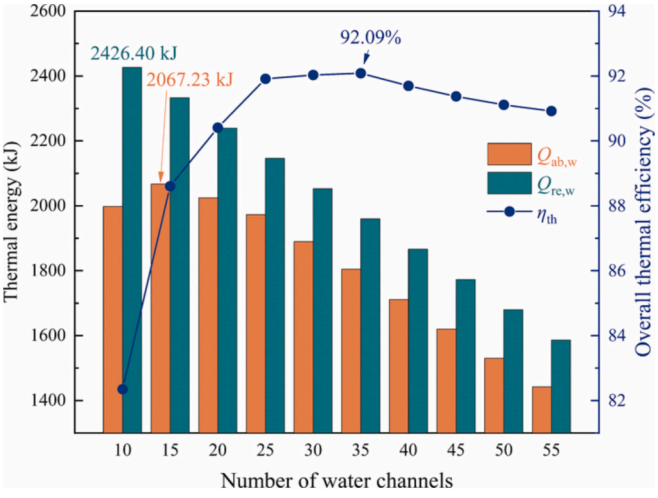

Fig. 10. The effect of number of the water channels on the amount of heat absorbed by the waterflow, the amount of heat released by the TCES composite materials and system's overall thermal efficiency.

5.5. Effect of width of the water channels

In this section, we investigate how the width of the water channels in HEX, denoted as "*w*", influence the system performance during the discharging process while maintaining a constant reactor volume and inlet parameters. Fig. 11 illustrates the relationship between *w* and the highest temperature of HEX outlet waterflow. It is observed that as *w* increases, the highest temperature of HEX outlet waterflow shows a decreasing trend. For instance, when *w* is set to 0.002 m (i.e., $V_s = 3.64$ L), the HEX achieves the maximum highest temperature of HEX outlet waterflow of 31.78 °C. However, with an increase in *w* to 0.025 m (i.e., $V_s = 0.42$ L), there is a significant decline, and the highest temperature of HEX outlet waterflow drops to 28.37 °C. This phenomenon can be attributed to the increase in the thermal resistance caused by the elongation of the heat transfer path as the water channel width expands. Furthermore, the widening of the water channel leads to a reduction in the volume of TCES composite material within reaction bed. Consequently, there is a decrease in the amount of heat released during the discharging process. Fig. 12 visually demonstrates the impact of the water channel width on the amount of heat released by the TCES composite materials and the amount of heat absorbed by the waterflow.

As shown in Fig. 12, when *w* increases from 0.002 m to 0.025 m, the amount of heat released by the TCES composite materials decreases from 2426.40 kJ to 279.97 kJ, and the amount of heat absorbed by the waterflow diminishes from 1998.17 kJ to 158.81 kJ. The system's overall thermal efficiency is intricately linked to the combined effects of the amount of heat released by the TCES composite materials and the amount of heat absorbed by the waterflow, as demonstrated in Fig. 12. The system's overall thermal efficiency gradually improves as *w* increases from 0.002 m until it reaches its peak of 83.88 % at $w = 0.015$ m (i.e., $V_s = 1.82$ L). However, a further increase in *w* leads to a rapid decline in the system's overall thermal efficiency, dropping to 66.37 % when *w* is 0.025.

Typically, the width of the water channels (i.e., flat microchannel tubes) falls within the range of 0.01 m or below. Based on the above-mentioned findings, a variation in *w* within this range, does not exert a

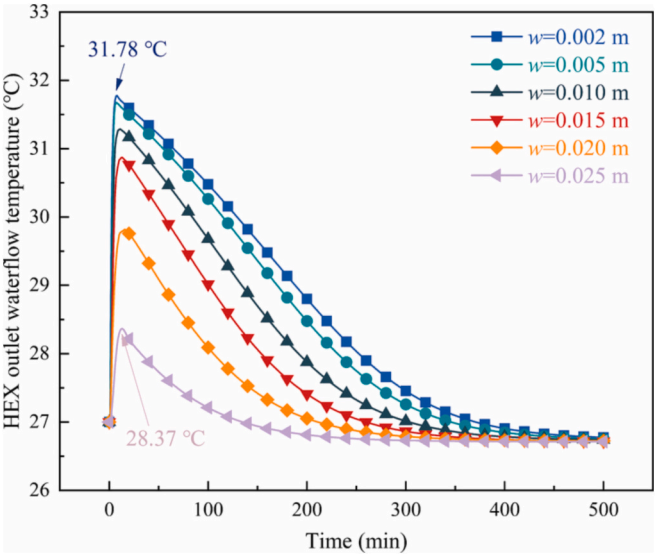

Fig. 11. The effect of width of the water channels on the HEX outlet waterflow temperature.

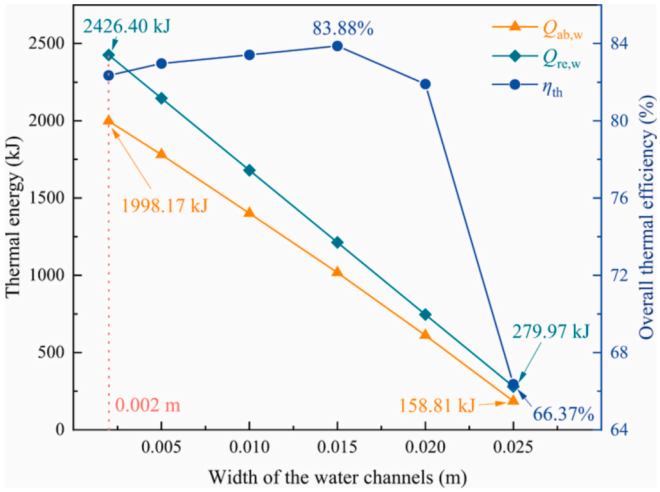

Fig. 12. The effect of width of the water channels on the amount of heat absorbed by the waterflow, the amount of heat released by the TCES composite materials and system's overall thermal efficiency.

substantial influence on the HEX outlet waterflow temperature and the system's overall thermal efficiency. Nevertheless, from the perspective of the amount of heat absorbed by the waterflow and the amount of heat released by the TCES composite materials, a smaller value of w is preferred to optimize system performance.

6. Conclusion

In this study, a TCES-HEX-HRU system was evaluated, integrating a TCES reactor with a water-to-air microchannel tube heat exchanger (HEX) and an air-to-air heat recovery unit (HRU). A comparison was made with a TCES-HEX system and a TCES-only system. Additionally, a parametric study was conducted, yielding the following conclusions:

(1) By adding the HRU to the TCES-HEX-HRU system, the overall thermal efficiency improved significantly (by 69 percentage points to 82.35 %) compared to the TCES-HEX system. While the TCES-HEX-HRU system had a slightly lower overall thermal efficiency (15.44 percentage points) compared to the TCES-only system, it addressed practical challenges effectively.
(2) Inlet airflow and HEX inlet water temperatures significantly affected the TCES-HEX-HRU system's maximum temperature lift and overall thermal efficiency. Raising the inlet airflow temperature improved performance, whereas higher HEX inlet water temperature had the opposite effect.
(3) Water flow velocity in the water channels had a significant impact on the HEX's maximum temperature lift, while airflow mass flow rate had negligible influence. Maintaining airflow mass flow rate below 0.0095 $kg{\cdot}s^{-1}$ and water flow rate below 0.004 $kg{\cdot}s^{-1}$ is crucial to balance maximum temperature lift and overall thermal efficiency.
(4) The quantity of water channels in the HEX significantly impacts the performance of the TCES-HEX-HRU system. Increasing the number of channels initially raises the maximum outlet water temperature, reaching 33.67 °C with 30 channels. However, further channel increments cause a decrease in outlet water temperature. The rise in channel quantity enhances the overall thermal efficiency, peaking at 92.09 % with 35 channels but exceeding this threshold reduces overall efficiency.
(5) Expanding HEX channel width lowers outlet water temperature, with a substantial 3.41 °C drop from 0.002 m to 0.025 m. Adjusting channel width within the standard range (0.002–0.01 m) minimally affects system thermal efficiency, consistently exceeding 83 %. Wider channels reduce heat absorption by water flow by the due to reduced TCES composite materials volume.

In summary, the TCES-HEX-HRU system outperforms both the TCES-only and TCES-HEX systems, considering comprehensive factors, and is influenced by inlet parameter and structure configuration. The primary objective of this study was to investigate the behaviour of the HEX unit during the discharging process and explore the feasibility of an open water-based TCES system. Although the TCES-HEX-HRU system discussed in this paper is not yet ready for real-world applications, the findings provide valuable insights for the design and operation of full-scale system. Based on the findings of this study, it can be concluded that the proposed water-based open TCES system is feasible and efficient for space heating in buildings. Future research will focus on the development of a full-scale TCES-HEX-HRU system with multilayer reactor bed modules to evaluate its practical performance. Additionally, the integration of this novel system into buildings for real-world environmental testing and cost-benefit analysis is planned.

CRediT authorship contribution statement

Yong Zhang: Software, Formal analysis, Investigation, Writing – original draft, Writing – review & editing. **Mingke Hu:** Conceptualization, Supervision, Methodology, Formal analysis, Investigation, Writing – review & editing. **Ziwei Chen:** Formal analysis, Writing – review & editing. **Yuehong Su:** Conceptualization, Supervision, Project administration, Funding acquisition, Writing – review & editing. **Saffa Riffat:** Resources, Project administration, Writing – review & editing.

Declaration of competing interest

The authors declare that they have no known competing financial interests or personal relationships that could have appeared to influence the work reported in this paper.

Data availability

Data will be made available on request.

Acknowledgements

The authors would like to acknowledge the Engineering and Physical Sciences Research Council (grant number: EP/T021233/1) for the financial support to this research.

References

[1] The global energy crisis – World Energy Outlook 2022 – Analysis-IEA, (n.d.). https://www.iea.org/reports/world-energy-outlook-2022/the-global-energy-crisis (accessed February 2, 2023).
[2] L.G. Swan, V.I. Ugursal, Modeling of end-use energy consumption in the residential sector: A review of modeling techniques, Renew. Sust. Energ. Rev. 13 (2009) 1819–1835, https://doi.org/10.1016/J.RSER.2008.09.033.
[3] J. Allen, A. Beaumont, M. Custard, H. Garrett, A. Gemmell, S. Kamal, S. Margoles, E. Munkley, F. Taylor, EFUS: Household Energy Consumption and Affordability, 2021.
[4] Heating–Analysis-IEA, (n.d.). https://www.iea.org/reports/heating (accessed February 2, 2023).
[5] National Energy Action (NEA)|Energy Crisis, (n.d.). https://www.nea.org.uk/energy-crisis/ (accessed February 3, 2023).
[6] J. Da, M. Li, G. Li, Y. Wang, Y. Zhang, Simulation and experiment of a photovoltaic—air source heat pump system with thermal energy storage for heating and domestic hot water supply, in: Build Simul, 2023, https://doi.org/10.1007/s12273-022-0960-6.
[7] R. Han, S. Xing, X. Wu, C. Pang, S. Lu, Y. Su, Q. Liu, C. Song, J. Gao, Relevant influence of alkali carbonate doping on the thermochemical energy storage of Ca-based natural minerals during CaO/CaCO3 cycles, Renew. Energy 181 (2022) 267–277, https://doi.org/10.1016/J.RENENE.2021.09.021.
[8] A. Fopah Lele, F. Kuznik, O. Opel, W.K.L. Ruck, Performance analysis of a thermochemical based heat storage as an addition to cogeneration systems, Energy Convers. Manag. 106 (2015) 1327–1344, https://doi.org/10.1016/j.enconman.2015.10.068.

[9] D. Wang, H. Liu, Y. Wang, K. Liu, Y. Liu, M. Gao, J. Fan, Thermal performance and evaluation of a novel stratified and mixed flexible transformation solar heat storage unit, in: Build Simul, 2022, https://doi.org/10.1007/s12273-022-0930-z.

[10] B. Zalba, J.M. Marín, L.F. Cabeza, H. Mehling, Review on thermal energy storage with phase change: materials, heat transfer analysis and applications, Appl. Therm. Eng. 23 (2003) 251–283, https://doi.org/10.1016/S1359-4311(02)00192-8.

[11] X. Zhang, S. Zhou, W. Liu, Z. Zhou, Y. Yang, Fabrication of structure-improved, sintering-resistant Li4SiO4 materials for stabilized thermochemical energy storage in concentrated solar power plants, J. Energy Storage 70 (2023), 108078, https://doi.org/10.1016/J.EST.2023.108078.

[12] B. Michel, N. Mazet, S. Mauran, D. Stitou, J. Xu, Thermochemical process for seasonal storage of solar energy: characterization and modeling of a high density reactive bed, Energy 47 (2012) 553–563, https://doi.org/10.1016/J.ENERGY.2012.09.029.

[13] J. Lin, Q. Zhao, H. Huang, H. Mao, Y. Liu, Y. Xiao, Applications of low-temperature thermochemical energy storage systems for salt hydrates based on material classification: a review, Sol. Energy 214 (2021) 149–178, https://doi.org/10.1016/J.SOLENER.2020.11.055.

[14] D. Aydin, S.P. Casey, S. Riffat, The latest advancements on thermochemical heat storage systems, Renew. Sust. Energ. Rev. 41 (2015) 356–367, https://doi.org/10.1016/J.RSER.2014.08.054.

[15] L.F. Cabeza, A. Solé, C. Barreneche, Review on sorption materials and technologies for heat pumps and thermal energy storage, Renew. Energy 110 (2017) 3–39, https://doi.org/10.1016/J.RENENE.2016.09.059.

[16] W. Chen, W. Li, Y. Zhang, Analysis of thermal deposition of MgCl2·6H2O hydrated salt in the sieve-plate reactor for heat storage, Appl. Therm. Eng. 135 (2018) 95–108, https://doi.org/10.1016/j.applthermaleng.2018.02.043.

[17] H. Ait Ousaleh, S. Sair, S. Mansouri, Y. Abboud, M. Zahouily, A. Faik, A. el Bouari, Enhanced inorganic salts stability using bentonite clay for high-performance and low-cost thermochemical energy storage, J. Energy Storage 49 (2022), https://doi.org/10.1016/J.EST.2022.104140.

[18] B. Ding, C. Xu, Z. Liao, F. Ye, Study on long-term thermochemical thermal storage performance based on SrBr2-expanded vermiculite composite materials, J. Energy Storage 42 (2021), https://doi.org/10.1016/j.est.2021.103081.

[19] Q. Miao, Y. Zhang, X. Jia, L. Tan, Y. Ding, MgSO4-expanded graphite composites for mass and heat transfer enhancement of thermochemical energy storage, Sol. Energy 220 (2021) 432–439, https://doi.org/10.1016/J.SOLENER.2021.03.008.

[20] K.E. N'Tsoukpoe, T. Schmidt, H.U. Rammelberg, B.A. Watts, W.K.L. Ruck, A systematic multi-step screening of numerous salt hydrates for low temperature thermochemical energy storage, Appl. Energy 124 (2014) 1–16, https://doi.org/10.1016/j.apenergy.2014.02.053.

[21] S. Wei, W. Zhou, R. Han, J. Gao, G. Zhao, Y. Qin, C. Wang, Influence of minerals with different porous structures on thermochemical heat storage performance of CaCl2-based composite sorbents, Sol. Energy Mater. Sol. Cells 243 (2022), 111769, https://doi.org/10.1016/J.SOLMAT.2022.111769.

[22] Q. Touloumet, L. Silvester, L. Bois, G. Postole, A. Auroux, Water sorption and heat storage in CaCl2 impregnated aluminium fumarate MOFs, Sol. Energy Mater. Sol. Cells 231 (2021), https://doi.org/10.1016/j.solmat.2021.111332.

[23] A. Fopah-Lele, J.G. Tamba, A review on the use of SrBr2·6H2O as a potential material for low temperature energy storage systems and building applications, Sol. Energy Mater. Sol. Cells 164 (2017) 175–187, https://doi.org/10.1016/J.SOLMAT.2017.02.018.

[24] W. Li, H. Guo, M. Zeng, Q. Wang, Performance of SrBr2·6H2O based seasonal thermochemical heat storage in a novel multilayered sieve reactor, Energy Convers. Manag. 198 (2019), https://doi.org/10.1016/j.en-conman.2019.111843.

[25] R. Fisher, Y. Ding, A. Sciacovelli, Hydration kinetics of K2CO3, MgCl2 and vermiculite-based composites in view of low-temperature thermochemical energy storage, J. Energy Storage 38 (2021), https://doi.org/10.1016/j.est.2021.102561.

[26] M. Gaeini, A.L. Rouws, J.W.O. Salari, H.A. Zondag, C.C.M. Rindt, Characterization of microencapsulated and impregnated porous host materials based on calcium chloride for thermochemical energy storage, Appl. Energy 212 (2018) 1165–1177, https://doi.org/10.1016/J.APENERGY.2017.12.131.

[27] L.C. Sögütoglu, P.A.J. Donkers, H.R. Fischer, H.P. Huinink, O.C.G. Adan, In-depth investigation of thermochemical performance in a heat battery: cyclic analysis of K2CO3, MgCl2 and Na2S, Appl. Energy 215 (2018) 159–173, https://doi.org/10.1016/J.APENERGY.2018.01.083.

[28] Cupric Chloride|Cl2Cu|CID 24014-Pub Chem, (n.d.). https://pubchem.ncbi.nlm.nih.gov/com- pound/Cupric-Chloride (accessed October 11, 2023).

[29] R.J. Clark, G. Gholamibozanjani, J. Woods, S. Kaur, A. Odukomaiya, S. Al-Hallaj, M. Farid, Experimental screening of salt hydrates for thermochemical energy storage for building heating application, J. Energy Storage 51 (2022), 104415, https://doi.org/10.1016/J.EST.2022.104415.

[30] L. Glasser, Thermodynamics of inorganic hydration and of humidity control, with an extensive database of salt hydrate pairs, J. Chem. Eng. Data 59 (2014) 526–530, https://doi.org/10.1021/JE401077X/SUPPL_FILE/JE401077X_SI_001.PDF.

[31] Y. Zhang, R. Wang, Sorption thermal energy storage: concept, process, applications and perspectives, Energy Storage Mater. 27 (2020) 352–369, https://doi.org/10.1016/J.ENSM.2020.02.024.

[32] Q. Wang, Y. Xie, B. Ding, G. Yu, F. Ye, C. Xu, Structure and hydration state characterizations of MgSO4-zeolite 13x composite materials for long-term thermochemical heat storage, Sol. Energy Mater. Sol. Cells 200 (2019), 110047, https://doi.org/10.1016/J.SOLMAT.2019.110047.

[33] S.P. Casey, J. Elvins, S. Riffat, A. Robinson, Salt impregnated desiccant matrices for 'open' thermo- chemical energy storage—selection, synthesis and characterisation of candidate materials, Energy Build. 84 (2014) 412–425, https://doi.org/10.1016/J.ENBUILD.2014.08.028.

[34] D. Zhu, H. Wu, S. Wang, Experimental study on composite silica gel supported CaCl2 sorbent for low grade heat storage, Int. J. Therm. Sci. 45 (2006) 804–813, https://doi.org/10.1016/J.IJTHERMALSCI.2005.10.009.

[35] T. Yan, C.Y. Wang, D. Li, Performance analysis of a solid-gas thermochemical composite sorption system for thermal energy storage and energy upgrade, Appl. Therm. Eng. 150 (2019) 512–521, https://doi.org/10.1016/J.APPLTHERMALENG.2019.01.004.

[36] R.J. Clark, A. Mehrabadi, M. Farid, State of the art on salt hydrate thermochemical energy storage systems for use in building applications, J. Energy Storage 27 (2020), 101145, https://doi.org/10.1016/J.EST.2019.101145.

[37] Y.J. Zhao, R.Z. Wang, Y.N. Zhang, N. Yu, Development of SrBr2 composite sorbents for a sorption thermal energy storage system to store low-temperature heat, Energy 115 (2016) 129–139, https://doi.org/10.1016/J.ENERGY.2016.09.013.

[38] Y.N. Zhang, R.Z. Wang, Y.J. Zhao, T.X. Li, S.B. Riffat, N.M. Wajid, Development and thermochemical characterizations of vermiculite/SrBr2 composite sorbents for low-temperature heat storage, Energy 115 (2016) 120–128, https://doi.org/10.1016/J.ENERGY.2016.08.108.

[39] A. Sapienza, I.S. Glaznev, S. Santamaria, A. Freni, Y.I. Aristov, Adsorption chilling driven by low temperature heat: new adsorbent and cycle optimization, Appl. Therm. Eng. 32 (2012) 141–146, https://doi.org/10.1016/J.APPLTHERMALENG.2011.09.014.

[40] E. Courbon, P. D'Ans, A. Permyakova, O. Skrylnyk, N. Steunou, M. Degrez, M. Frère, Further improvement of the synthesis of silica gel and CaCl2 composites: enhancement of energy storage density and stability over cycles for solar heat storage coupled with space heating applications, Sol. Energy 157 (2017) 532–541, https://doi.org/10.1016/J.SOLENER.2017.08.034.

[41] S.P. Casey, D. Aydin, S. Riffat, J. Elvins, Salt impregnated desiccant matrices for "open" thermoche- mical energy storage - hygrothermal cyclic behaviour and energetic analysis by physical experimentation, Energy Build. 92 (2015) 128–139, https://doi.org/10.1016/j.enbuild.2015.01.048.

[42] W. Li, J.J. Klemeš, Q. Wang, M. Zeng, Energy storage of low potential heat using lithium hydroxide based sorbent for domestic heat supply, J. Clean. Prod. 285 (2021), 124907, https://doi.org/10.1016/J.JCLEPRO.2020.124907.

[43] C. Wang, H. Yang, B. Nie, B. Zou, Z. Li, J. Han, L. Tong, L. Wang, Y. Ding, Discharging behavior of a shell-and-tube based thermochemical reactor for thermal energy storage: modeling and experimental validation, Int. J. Heat Mass Transf. 183 (2022), https://doi.org/10.1016/J.IJHEATMASSTRANSFER.2021.122160.

[44] A. Mukherjee, A. Shankar Pujari, S.N. Shinde, U. Kashyap, L. Kumar, C. Subramaniam, S.K. Saha, Performance assessment of open thermochemical energy storage system for seasonal space heating in highly humid environment, Renew. Energy 201 (2022) 960–1481, https://doi.org/10.1016/j.renene.2022.10.075.

[45] B. Michel, P. Neveu, N. Mazet, Comparison of closed and open thermochemical processes, for long-term thermal energy storage applications, Energy 72 (2014) 702–716, https://doi.org/10.1016/J.ENERGY.2014.05.097.

[46] A. Solé, I. Martorell, L.F. Cabeza, State of the art on gas–solid thermochemical energy storage systems and reactors for building applications, Renew. Sust. Energ. Rev. 47 (2015) 386–398, https://doi.org/10.1016/J.RSER.2015.03.077.

[47] W. Li, J.J. Klemeš, Q. Wang, M. Zeng, Salt hydrate–based gas-solid thermochemical energy storage: current progress, challenges, and perspectives, Renew. Sust. Energ. Rev. 154 (2022), 111846, https://doi.org/10.1016/J.RSER.2021.111846.

[48] A.H. Abedin, M.A. Rosen, Closed and open thermochemical energy storage: energy- and exergy-based comparisons, Energy 41 (2012) 83–92, https://doi.org/10.1016/J.ENERGY.2011.06.034.

[49] A. Fopah-Lele, C. Rohde, K. Neumann, T. Tietjen, T. Rönnebeck, K.E. N'Tsoukpoe, T. Osterland, O. Opel, W.K.L. Ruck, Lab-scale experiment of a closed thermochemical heat storage system including honeycomb heat exchanger, Energy 114 (2016) 225–238, https://doi.org/10.1016/j.energy.2016.08.009.

[50] B. Michel, N. Mazet, P. Neveu, Experimental investigation of an innovative thermochemical process operating with a hydrate salt and moist air for thermal storage of solar energy: global performance, Appl. Energy 129 (2014) 177–186, https://doi.org/10.1016/J.APENERGY.2014.04.073.

[51] H. Zhang, S. Liu, A. Shukla, Y. Zou, X. Han, Y. Shen, L. Yang, P. Zhang, K. Kusakana, Thermal performance study of thermochemical reactor using net-packed method, Renew. Energy 182 (2022) 483–493, https://doi.org/10.1016/J.RENENE.2021.09.115.

[52] Q. Zhao, J. Lin, H. Huang, Q. Wu, Y. Shen, Y. Xiao, Optimization of thermochemical energy storage systems based on hydrated salts: a review, Energy Build. 244 (2021), 111035, https://doi.org/10.1016/J.EN-BUILD.2021.111035.

[53] D. Aydin, S.P. Casey, X. Chen, S. Riffat, Numerical and experimental analysis of a novel heat pump driven sorption storage heater, Appl. Energy 211 (2018) 954–974, https://doi.org/10.1016/J.APENERGY.2017.11.102.

[54] Y. Zhang, M. Hu, Z. Chen, Y. Su, S. Riffat, Modelling analysis of a solar-driven thermochemical energy storage unit combined with heat recovery, Renew. Energy 206 (2023) 722–737, https://doi.org/10.1016/J. RENENE.2023.02.076.

[55] Central Heating System: Everything You Need to Know | Boiler Guide, (n.d.). https://www.boiler-guide.co.uk/articles/central-heating-systems (accessed February 13, 2023).

[56] D. Aydin, S.P. Casey, X. Chen, S. Riffat, Novel "open-sorption pipe" reactor for solar thermal energy storage, Energy Convers. Manag. 121 (2016) 321–334, https://doi.org/10.1016/j.enconman.2016.05.045.

[57] A. Fopah Lele, F. Kuznik, H.U. Rammelberg, T. Schmidt, W.K.L. Ruck, Thermal decomposition kinetic of salt hydrates for heat storage systems, Appl. Energy 154 (2015) 447–458, https://doi.org/10.1016/j.apenergy.2015.02.011.

[58] R. Olives, S. Mauran, A highly conductive porous medium for solid-gas reactions: effect of the dispersed phase on the thermal tortuosity, Transp. Porous Media 43 (2001) 377–394, https://doi.org/10.1023/A:1010780623891/METRICS.
[59] A. Malley-Ernewein, S. Lorente, Constructal design of thermochemical energy storage, Int. J. Heat Mass Transf. 130 (2019) 1299–1306, https://doi.org/10.1016/J.IJHEATMASSTRANSFER.2018.10.097.
[60] M. Hu, B. Zhao, X. Ao, X. Ren, J. Cao, Q. Wang, Y. Su, G. Pei, Performance assessment of a trifunctional system integrating solar PV, solar thermal, and radiative sky cooling, Appl. Energy 260 (2020), 114167, https://doi.org/10.1016/J.APENERGY.2019.114167.
[61] D.P. Bentz, F. Zunino, D. Lootens, Chemical vs. physical acceleration of cement hydration, Concr. Int. 38 (2016) 37. /pmc/articles/PMC5220402/ (accessed October 23, 2023).
[62] E.A. Levitskij, Y.I. Aristov, M.M. Tokarev, V.N. Parmon, "Chemical heat accumulators": a new approach to accumulating low potential heat, Sol. Energy Mater. Sol. Cells 44 (1996) 219–235, https://doi.org/10.1016/0927-0248(96)00010-4.
[63] M.W. Chase, M.W. Chase, NIST-JANAF thermochemical tables for the bromine oxides, JANAF thermochemical tables. I. Ten organic molecules related to atmospheric chemistry, J. Phys. Chem. Ref. Data 25 (1996) 475, https://doi.org/10.1063/1.555994.